Synchronization Strategy Based on Resonant Current Detection for Bidirectional Wireless Charging System

Dongbo Zhang, Min Chen, *Member, IEEE*, Bodong Li, Xiaoqing Wang, *Student Member, IEEE*, Xinnan Sun, and Feng Jiang

***Abstract*—Bidirectional wireless power transfer greatly improves the reliability of power supply. However, wireless communication between the primary and pickup controllers is usually required to transmit load information, which has time delay and is easily interfered by electromagnetic fields. Existing solutions to avoid the use of communication can be divided into three categories: additional dc/dc circuit, primary side bridge control, and secondary side bridge control. Compared with the other two methods, the secondary side bridge control has low loss and good robustness. But, it usually requires phase-locked loop (PLL) to eliminate the frequency error between primary and secondary side bridges, which increases the complexity. In this article, a constant current control strategy without communication is proposed. It is based on the secondary side bridge control and the switching sequence of the secondary side bridge is periodically synchronized according to the phase of the resonant current. It works robustly without the need for additional hardware such as PLL or Multiplier. The harmonic sensitivity analysis, parameter optimization design and stability analysis are carried out to improve the control efficiency. Experimental results based on a 1 kW prototype with dual *LCC* resonant network are presented to verify the effectiveness of the proposed control strategy.**

***Index Terms*—Bidirectional wireless charging, *LCC*, non-communication.**

NOMENCLATURE

L_1	Compensation inductor of primary side.
L_2	Compensation inductor of secondary side.
L_p	Self-inductance of the transmitting coil.
L_s	Self-inductance of the receiving coil.
M	Mutual inductance between L_p and L_s.
k	Coupling coefficient.
i_s	Output current of secondary resonant network.
I_{s_nth}	The amplitude of the *n-th* harmonic current in i_s.
i_p	Input current of primary resonant network.
i_o	Load current.
v_p	Input voltage of primary resonant network.
v_s	Input voltage of secondary resonant network.
V_{p_nth}	Amplitude of the *nth* harmonic voltage in v_p.
V_{s_nth}	Amplitude of the *nth* harmonic voltage in v_s.
ω_0	Resonant angular frequency.
T_0	Resonant period of resonant network.
T_p	Switching period of primary side bridge.
T_s	Switching period of secondary side bridge.
ΔT	Difference between T_p and T_s.
θ_p	Phase shift of primary side bridge.
θ_s	Phase shift of secondary side bridge.
θ	Relative phase angle of v_s leading v_p.
Δt_0	Time corresponding to the initial value of θ.
φ	Phase difference between v_s and i_s.
φ_i	φ in the *ith* switching cycle after the synchronization point.
T_C	Synchronization period.
$S_5 \sim S_8$	Secondary side MOSFETs.
P_{TC}	Average active power in T_C.
Q_{TC}	Average reactive power in T_C.
r	Reference value of the ratio of Q_{TC} to P_{TC}.
X_{L1}	Impedance of inductance L_1.

Manuscript received February 22, 2022; revised March 28, 2022; accepted April 19, 2022. Date of publication April 25, 2022; date of current version May 23, 2022. This work is supported by National Key R&D Program under Grant 2020YFB1506800. Recommended for publication by Associate Editor J. Acero. *(Corresponding author: Min Chen.)*

The authors are with the Department of Applied Electronics, Zhejiang University, Hangzhou 310027, China, and also with ZJU-Hangzhou Global Scientific and Technological Innovation Center, Hangzhou 311200, China (e-mail: 22010073@zju.edu.cn; calim@zju.edu.cn; bodong_li@zju.edu.cn; 11710013@zju.edu.cn; 3150103575@zju.edu.cn; jiangfeng@zju.edu.cn).

Color versions of one or more figures in this article are available at https://doi.org/10.1109/TPEL.2022.3169882.

Digital Object Identifier 10.1109/TPEL.2022.3169882

I. INTRODUCTION

TRADITIONAL power supply has been realized through cable since the advent of electric energy, but it will cause problems, such as cable aging and interface wear. The harsh working conditions, the wear and corrosion of the interface will greatly reduce the safety [1]. In contrast, wireless charging effectively solves these problems and makes charging more convenient and flexible. Meanwhile, more and more scenarios are beginning to show the demand for bidirectional wireless power transfer (BWPT) technology, such as V2G technology [2]–[4] and portable devices charging [5], [6]. In the future, BWPT can also be used in new energy power generation and other occasions that require bidirectional energy flow.

In order to keep a constant power output, a bidirectional dc/dc circuit can be added to the input and output side [7]–[10]. The block diagram is shown in Fig. 1. The load-side dc–dc circuit can control the reference power, but it increases costs and losses

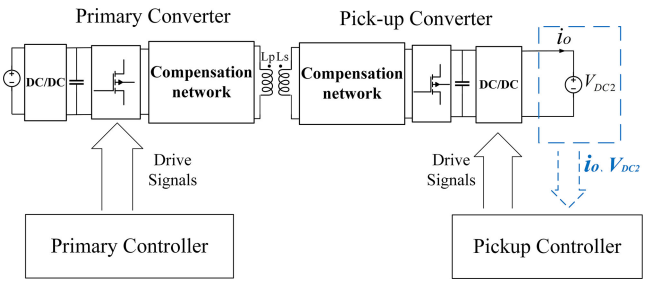

Fig. 1. System block diagram with dc/dc circuit.

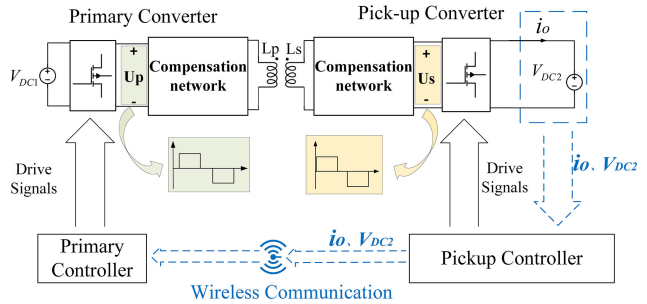

Fig. 2. Phase shift control system.

[11]–[13]. In contrast, the phase shift control strategy has been widely discussed and analyzed due to its flexible control method and simple hardware [14]–[21]. The block diagram is shown in Fig. 2. However, due to the current source characteristics of the resonant network [22], [23] and the uncertainty of the distance between the induction coils, wireless communication is needed to transmit the load information to the primary controller. This causes a delay of several milliseconds and is easily interfered by electromagnetic fields. Therefore, the use of communication in closed-loop control will reduce the stability of the system.

In order to avoid using wireless communication, the control strategies can be further divided into two categories: primary side bridge control and secondary side bridge control. When using the primary side bridge control, the transmission power is controlled by adjusting the switching frequency or phase shift of the primary side bridge. In [24], a MOSFET is added to the load side to maintain a constant output current. Then, the primary side detects the current change and adjusts the phase shift of the primary side to meet the load current. It uses the disturbance observation method, and the dynamic response speed needs to be further improved. A power-frequency droop control method is employed in [25]. The primary side detects the power disturbance generated by the secondary side, and the output power of the circuit is changed by adjusting the frequency. It extends the power transmission range, but the circulating current will increase at the non resonant frequency. In addition, the primary side bridge can control the output power by detecting the signal and calculating the load impedance [26]. Although the system structure is simple, it relies on theoretical calculation and signal detection. To sum up, the primary side bridge control detects the load signal indirectly, so the accuracy and dynamic performance are deficient. In addition, the secondary bridge works as the uncontrolled rectifier. It also increases the loss.

In contrast, the secondary side bridge control directly detects the output power for feedback, and then adjusts the operating mode of the secondary side bridge. It avoids the shortcomings of the primary bridge control. Mao *et al.* [27] proposed a phase angle control method with varactors and realized the adaptive deadtime control in the transmitter mode and the off-delay compensation in the receiver mode with delay-locked loop. The transmission efficiency of the whole working range is effectively improved. However, the regulation range of transmission power needs to be expanded. A reconfigurable rectifier is proposed in [28]. The secondary side bridge switches between the voltage doubling rectifier and the full bridge rectifier. The power is controlled by the working time ratio of the two modes. At the same time, the primary side can detect the disturbance of mode switching to assist in power control. The combination of primary and secondary side control effectively increases the power transmission range. However, the control strategy adds a switch for mode switching, and the discontinuity of gain in the two modes will increase the ripple.

In addition, the phase angle control of the secondary side bridge is widely used because of its flexible control. The relative phase angle between the primary and secondary side bridges needs to be maintained at $\pm 90^\circ$ to ensure that the transmitted reactive power is zero [29]. However, since the primary controller and pickup controller are independent, there will always be a slight error in the frequencies between the primary and secondary side bridges. This causes the periodic change of relative phase angle between primary and secondary side bridges, which will lead to transmission power oscillation. Therefore, PLL or VCO is used to eliminate the frequency error in [29]–[31]. In [29], an auxiliary coil is added on the secondary side to detect the phase of the primary side bridge, and then adjust the relative phase angle. However, the method requires accurate sampling compensation, and controlling the phase difference between the primary and secondary sides by $\pm 90^\circ$ cannot cope with the detuning situation [30]. In order to enhance the robustness, a synchronous control strategy based on disturbance observation method is proposed in [32]. Disturbance is applied to the relative phase angle. If the power increases, the relative phase angle will continue to increase or decrease in the same direction. Otherwise it will change in the opposite direction. This strategy can avoid the influence of parameter error and detuning, but the power will fluctuate all the time affected by disturbance, which will also affect the stability. Furthermore, a more practical method is to adjust the phase angle of the secondary side bridge by detecting the active and reactive power output by the secondary resonant network [30], [31]. The reactive power is detected to carry out the control of PLL, so as to eliminate the frequency error and keep the reactive power at 0. It effectively avoids interference caused by component parameter errors. However, complex hardware circuits (voltage and current sensors, phase-shifting circuits and multipliers) are required to calculate active and reactive power. At the same time, the existence of harmonic component makes it difficult to detect reactive power accurately, which will lead to small control deviation.

Compared with the other methods, the phase angle control of the secondary side bridge has the advantages of low loss, high

TABLE I
CONTROL STRATEGY WITHOUT COMMUNICATION

Category	Control Strategy	Additional MOSFET	Parameter Variation Problem	Design complexity	PLL Requirement	Power fluctuation
Additional circuit	Additional bidirectional DC / DC circuit[7-10]	Yes	No	Low	No	No
Primary bridge control	Primary side control according to fluctuation generated by additional MOSFET on secondary side[24]	Yes	No	Low	No	Yes
	Load impedance calculation [26]	None	Yes	Low	No	No
Secondary bridge control	Secondary side bridge switches between the voltage doubling rectifier and the full bridge rectifier. The primary side detects the disturbance of mode switching to assist in power control [28]	Yes	No	Medium	No	Yes
	Phase detection by adding a mutual inductance coil on the secondary side [29]	None	Yes	High	Yes	No
	Adjust relative phase angle by perturbation observation method[32]	None	No	Low	No	Yes
	P and Q detection [30-31]	None	No	Medium	Yes	No
	Proposed method	**None**	**No**	**Low**	**No**	**No**

accuracy and good dynamic performance. However, it needs additional hardware to maintain the relative phase angle and eliminate the frequency difference. To solve these problems, this article proposed a strategy to correct the relative phase angle by detecting the output current of the resonator, which is robust and free of additional hardware. The proposed strategy regulates the active power by adjusting the phase shift of the secondary side bridge. The phase of the resonant current is detected in each synchronization period, and the switching sequence of secondary side bridge is synchronized accordingly. By designing the synchronization period, the drift of relative phase angle can be limited to a small range. In this way, constant active power can be transmitted when the reactive power is limited to a small amount.

The advantages and drawbacks of these methods are given in Table I. Compared with [29]–[32], the proposed method has no additional disturbance, does not require PLL, VCO, and complex detection circuits, and is not affected by detection error or parameter error. Section II introduces the phase shift control of dual *LCC* BWPT system, and presents the mathematical model to analyze the power oscillation caused by frequency deviation. Further details about the strategy and the design method of synchronization period are presented in Section III. The harmonic sensitivity and parameter optimization design for the proposed strategy are also analyzed. Generalized state space averaging (GSSA) method is used to analyze the stability. The effectiveness of the proposed control strategy is verified by the experimental results of a 1 kW BWPT prototype.

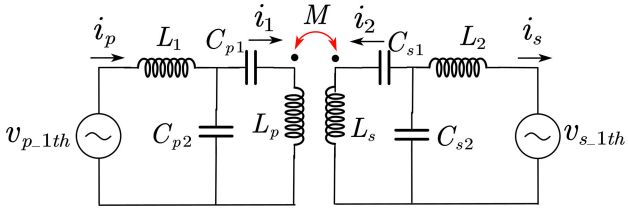

Fig. 3. Double *LCC* resonant network.

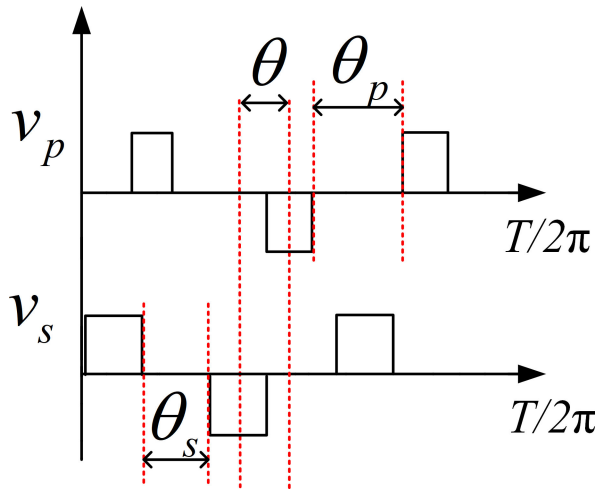

Fig. 4. Schematic diagram of phase shift angle.

II. BIDIRECTIONAL WIRELESS POWER TRANSFER SYSTEM

The diagram of BWPT system is depicted in Fig. 2. The power transmission characteristics will be introduced. The power oscillation caused by frequency difference between the primary and secondary side bridges will also be analyzed in this section.

A. Phase Shift Control Method

The resonant network of the BWPT system includes double *LCC*, double series–series compensated topology and so on. As the dual *LCC* resonant network has the advantages of high transmission power and good security, it is selected for research [33], [34], as shown in Fig. 3. v_{p_1th} and v_{s_1th} are the fundamental components of the voltage at both ends of the resonant network. L_P is the transmitting coil. L_S is the receiving coil, and M is the mutual inductance between L_P and L_S.

Fig. 4 shows the input voltage v_p on the primary side and v_s on the secondary side of the resonant network, where θ is the relative phase angle of v_s leading v_p, θ_p and θ_s are the phase shifts of primary and secondary side bridges.

The fundamental and harmonic components can be obtained by Fourier decomposition as

$$\begin{cases} v_p(t) = \sum\limits_{n=13,5\ldots}^{\infty} V_{p\_nth} \sin n\omega_0 t \\ \quad = \dfrac{4V_{\mathrm{DC1}}}{\pi} \sum\limits_{n=13,\ldots}^{\infty} \dfrac{1}{n} \cos\left(\dfrac{n}{2}\theta_p\right) \sin n\omega_0 t \\ v_s(t) = \sum\limits_{n=13,5\ldots}^{\infty} V_{s\_nth} \sin(n\omega_0 t + n\theta) \\ \quad = \dfrac{4V_{\mathrm{DC2}}}{\pi} \sum\limits_{n=13,\ldots}^{\infty} \dfrac{1}{n} \cos\left(\dfrac{n}{2}\theta_s\right) \sin(n\omega_0 t + n\theta) \end{cases} \tag{1}$$

where ω_0 is the resonant angular frequency, V_{p_nth} and V_{s_nth} are the amplitudes of the nth harmonic voltage in v_p and v_s respectively. Under the fundamental wave model, the current can be expressed as [34]

$$\begin{cases} i_p = \dfrac{MV_{s\_1th}}{\omega_0 L_1 L_2} \sin\left(\omega_0 t + \theta + \dfrac{\pi}{2}\right) \\ i_1 = \dfrac{V_{p\_1th}}{\omega_0 L_1} \sin\left(\omega_0 t - \dfrac{\pi}{2}\right) \\ i_s = \dfrac{MV_{p\_1th}}{\omega_0 L_1 L_2} \sin\left(\omega_0 t - \dfrac{\pi}{2}\right) \\ i_2 = \dfrac{V_{s\_1th}}{\omega_0 L_2} \sin\left(\omega_0 t + \theta - \dfrac{\pi}{2}\right) \end{cases}. \tag{2}$$

Combining (1) and (2), the transmitted power can be further calculated as

$$\begin{cases} P = -\frac{MV_{p\_1th}V_{s\_1th}}{2\omega_0 L_1 L_2} \sin\theta \\ \quad = -\dfrac{8MV_{\mathrm{DC1}}V_{\mathrm{DC2}}}{\pi^2\omega_0 L_1 L_2} \cos\dfrac{\theta_p}{2} \cos\dfrac{\theta_s}{2} \sin\theta \\ Q = -\dfrac{MV_{p\_1th}V_{s\_1th}}{2\omega_0 L_1 L_2} \cos\theta \\ \quad = -\dfrac{8MV_{\mathrm{DC1}}V_{\mathrm{DC2}}}{\pi^2\omega_0 L_1 L_2} \cos\dfrac{\theta_p}{2} \cos\dfrac{\theta_s}{2} \cos\theta \end{cases}. \tag{3}$$

According to (3), the transmission power can be adjusted by θ_p or θ_s. In order to keep the reactive power at 0, θ needs to be kept at $-90°$ when the power is transmitted forward. However, when the component parameters change or the circuit does not work at the resonance frequency, the ideal value of θ will change. The deviation of θ will increase the reactive power. On the other hand, there will always be a slight error in the frequencies between the primary and secondary side bridges since the primary and pickup controllers are independent. This causes the periodic change of θ, which will lead to transmission power oscillation.

B. Analysis of Power Oscillation

When there is an error between the primary switching period T_P and the secondary switching period T_S, θ will gradually change as shown in Fig. 5, where Δt_0 is the time corresponding to the initial relative phase angle and $\Delta T = T_P - T_S$.

Assuming that the resonant frequency of the compensation network is T_0, the error is small, so T_P and T_S are close to T_0. As shown in Fig. 5, the time corresponding to θ of the nth switching cycle is $\Delta t_0 + (n-1)\Delta T$. Therefore, θ can be given by

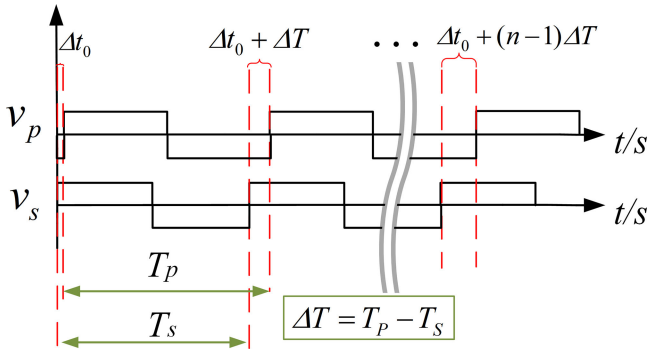

Fig. 5. Accumulation of phase error ($\theta_s = \theta_p = 0$).

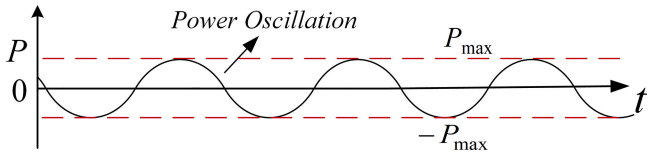

Fig. 6. Transmission power with frequency difference.

$$\theta = \frac{2\pi}{T_0}\left(\Delta t_0 + \frac{\Delta T}{T_0} t\right). \tag{4}$$

Substituting (4) into (3), the active and reactive power can be given by

$$\begin{cases} P = -\dfrac{MV_{p\_1th}V_{s\_1th}}{2\omega_0 L_1 L_2} \sin\left[\dfrac{2\pi}{T_0}\left(\Delta t_0 + \dfrac{\Delta T}{T_0} t\right)\right] \\ Q = -\dfrac{MV_{p\_1th}V_{s\_1th}}{2\omega_0 L_1 L_2} \cos\left[\dfrac{2\pi}{T_0}\left(\Delta t_0 + \dfrac{\Delta T}{T_0} t\right)\right] \end{cases}. \tag{5}$$

The waveform of P is shown in Fig. 6. It shows that the frequency difference will cause the transmitted active power to oscillate sinusoidally at a fixed frequency, and the average output power will be 0. The frequency difference leads to the continuous phase shift of the primary and secondary side bridges. Therefore, the essential cause of power oscillation is also the change of θ. If θ is kept stable, stable output power can be obtained. Therefore, a synchronization technology is needed in the control.

III. Proposed Control Strategy

In order to keep θ stable, one solution is to eliminate the frequency error and design a closed loop of reactive power [30], [31]. It will increase the complexity and the control effect will be reduced due to inaccurate reactive power detection. This article proposed a synchronization strategy to periodically correct θ by detecting the output current of the resonant network, which is much simpler and reliable. The frequency difference will slightly affect the transmission power in the proposed control strategy. Therefore, the transmission power is calculated accurately in Section III-B. At the same time, the control strategy relies on the detection of the current zero-crossing point. The harmonic current will affect the accuracy of the detection. Therefore, it is

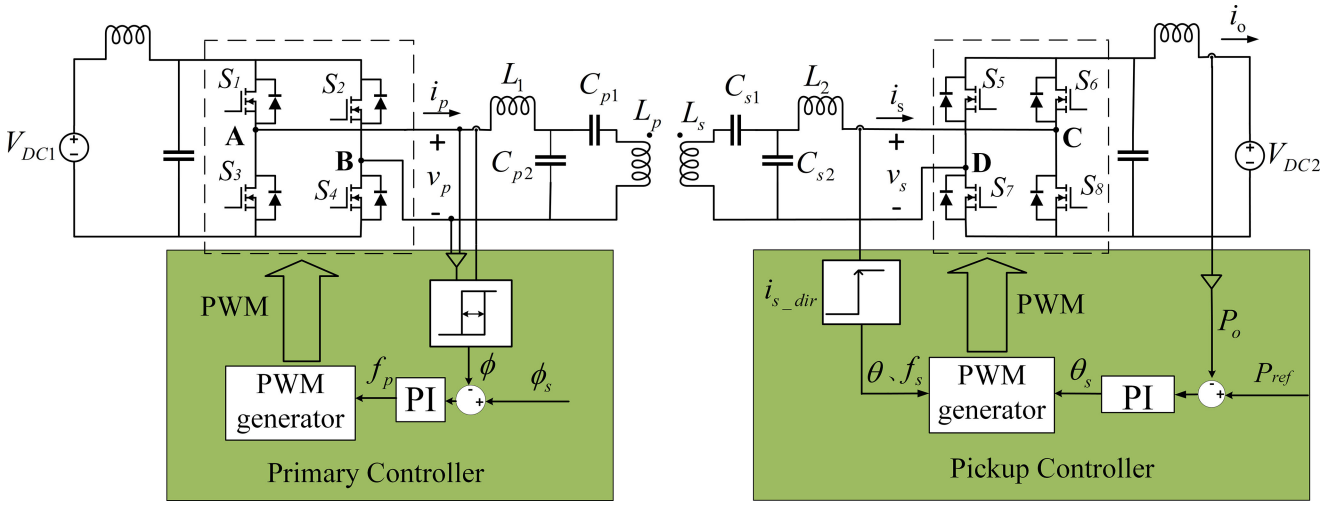

Fig. 7. Block diagram of the proposed control strategy.

necessary to establish the circuit model to analyze the harmonic sensitivity, which is shown in Section III-C.

A. Proposed Control Strategy

The system block diagram of the proposed control strategy is shown in Fig. 7. V_{DC1} and V_{DC2} are voltage sources. When the system starts to work, the secondary side bridge is not driven and its body diodes are used for rectification. The primary side tracks the resonant frequency by detecting the phase difference between v_p and i_p, and adjusts the switching frequency f_p of the primary side bridge. Thus, the phase difference between i_p and v_p is maintained at a reference value. Resonant frequency point tracking can avoid detuning caused by parameter errors.

At the same time, the pickup controller samples i_s to capture the zero-crossing point and calculate the frequency to obtain f_s. After f_s is stable, θ will remain at a fixed value. Then, the secondary side bridge will be driven and f_s will be used as its switching frequency. Taking into account the detection error and the difference between the controllers, there will be an error in the switching frequency between the primary and secondary side bridges. From (2), i_s lags v_p 90° and is independent of v_s. If v_s and i_s are in phase, θ will stabilize at −90°. Therefore, v_s can be periodically synchronized by detecting the phase of i_s, thereby avoiding power oscillation. The phase synchronization strategy is performed as Fig. 8. i_{s_dir} is the polarity signal of i_s and u_{g5} - u_{g8} are the driving signals of secondary side bridge. The pickup controller captures the rising edge of $i_{\mathrm{s\_dir}}$ and synchronizes θ at each synchronization point. The synchronization period T_C is N times the period of T_0 as (6), which means that synchronization operation occurs every N cycles of i_s.

$$T_C = NT_0. \tag{6}$$

At the synchronization point, v_s is corrected to be in phase with i_s. While synchronizing the secondary side bridge, the pickup controller detects the error between the output current and the reference value, and then adjusts θ_s through PI controller. As shown in Fig. 8, the secondary circuit has four stages in each switching cycle: I; II; III; and IV. Each stage is shown in Fig. 9. In stages I and III, the current resonates in the resonant network, while in stages II and IV, the current flows to the load. In order to complete the synchronization, the switching sequence at the synchronization point needs to be calculated. The synchronization process is as follows.

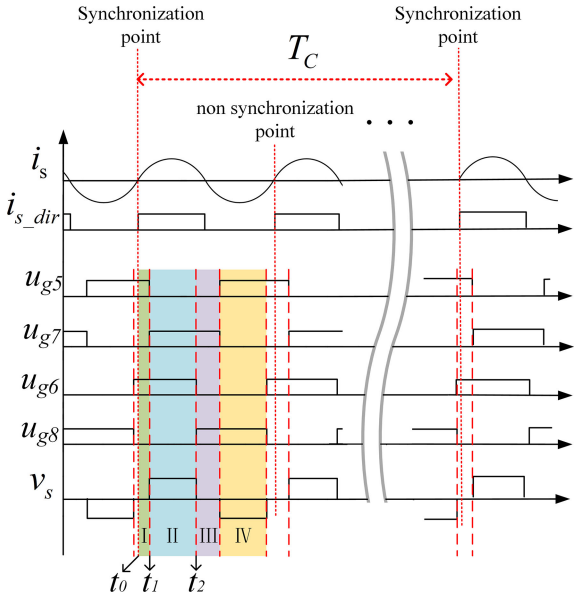

Fig. 8. Schematic diagram of secondary side bridge synchronization.

1) *Stage I [t_0, t_1]:* The pickup controller captures the rising edge of $i_{\mathrm{s\_dir}}$ at t_0 and starts to synchronize. During t_0-t_1, both S_5 and S_6 are turned ON. Therefore v_s is 0. S_5 is turned OFF at t_1, and the time from t_0 to t_1 can be presented as $t_1 - t_0 = \theta_s / (4\pi f_s)$.
2) *Stage II [t_1, t_2]:* At this stage, S_5 is in the OFF state, and S_6 is still ON. Therefore v_s is equal to V_{DC2}, and the resonant current flows to the load. S_6 is turned OFF at t_2, and the duration of state II is: $t_2 - t_1 = T_s / 2 - \theta_s / (2\pi f_s)$.

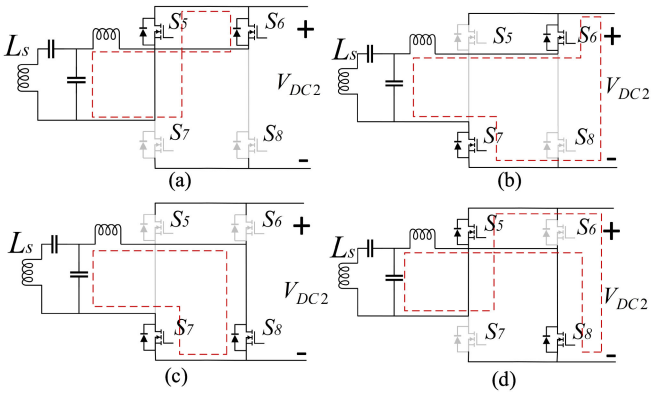

Fig. 9. Working stage of secondary circuit. (a) Stage I. (b) Stage II. (c) Stage III. (d) Stage IV.

Through the switching timing adjustment, v_s and i_s are always in phase in the first switching cycle after the synchronization point. After t_2, the secondary bridge still uses f_s as the switching frequency. Although there is still frequency error between the primary and secondary side bridges, the periodic synchronization can avoid large amplitude shift of θ.

In summary, the control strategy keeps θ stable through current detection. Therefore, constant power output can be achieved without wireless communication. θ is determined by the phase of i_s rather than the detection of θ or theoretical calculation, so it can deal with the non ideal working conditions caused by parameter errors and harmonics.

Due to the frequency deviation between the primary and the secondary side, the value of N will affect the transmitted active and reactive power. When N is too large, a lot of reactive power will be generated. At the same time, it is also necessary to consider the impact of harmonic currents on the synchronization process. These will be introduced in Section III-B and III-C. The stability analysis is presented with GSSA method in Section III-D.

B. Power Calculation and Design of Synchronization Period

According to the proposed strategy, the phases of v_s and i_s are slightly different at the non-synchronization point due to frequency error. It will produce reactive power and loss. The average active power transmitted is also changed. Therefore, the average active and reactive power need to be calculated, and N needs to be designed to reduce loss.

According to (5), the average active power P_{Tc} and reactive power Q_{Tc} in a synchronization period T_C can be calculated as

$$\begin{cases} Q_{T_C} = \dfrac{1}{N}\left(Q_1 + Q_2 \cdots + Q_N\right) = \dfrac{S}{N}\displaystyle\sum_{i=1}^{N} \sin\varphi_i \\ P_{T_C} = \dfrac{1}{N}\left(P_1 + P_2 \cdots + P_N\right) = \dfrac{S}{N}\displaystyle\sum_{i=1}^{N} \cos\varphi_i \end{cases} \tag{7}$$

where $Q_1 \sim Q_N$ and $P_1 \sim P_N$ are the reactive and active power generated in each switching cycle after the synchronization point respectively, S is the apparent power, and φ_i is the phase difference between v_s and i_s in the ith switching cycle after the synchronization point. They can be obtained from (3)–(5)

$$\begin{cases} S = \sqrt{P^2 + Q^2} = \dfrac{M V_{p\_1th} V_{s\_1th}}{2\omega_0 L_1 L_2} \\ \varphi_i = \dfrac{\Delta T}{T_0} * 2\pi * (i-1)\,(i = 1, \ldots, N) \end{cases} \tag{8}$$

where Q_{Tc} is the average value of $Q_1 \sim Q_N$, and $Q_1 \sim Q_N$ has the same calculation form. Therefore, Q_{Tc} can be approximated by integration as

$$\begin{aligned} Q_{T_C} &= \frac{S}{N}\int_0^N \sin\left(\frac{\Delta T}{T_0} * 2\pi t\right) dt \\ &= \frac{S T_0}{2\pi N \Delta T}\left[1 - \cos\left(\frac{\Delta T}{T_0} * 2\pi N\right)\right]. \end{aligned} \tag{9}$$

Similarly, P_{T_C} can be calculated as

$$P_{T_C} = \frac{S T_0}{2\pi N \Delta T}\ \sin\left(\frac{\Delta T}{T_0} * 2\pi N\right). \tag{10}$$

It can be seen from (10) that with the increase of N, P_{Tc} decreases and Q_{Tc} increases. Then the ratio of Q_{Tc} to P_{Tc} can be calculated as

$$\frac{Q_{T_C}}{P_{T_C}} = \tan\left(\frac{\Delta T}{T_0} * \pi N\right). \tag{11}$$

The ratio of Q_{Tc} to P_{Tc} increases as N increases. In order to reduce the loss, N needs to have an appropriate value range. Assuming that the maximum allowable ratio of Q_{Tc} to P_{Tc} is r, the range of N can be given by

$$N < \frac{T_0}{\pi \Delta T}\arctan(r). \tag{12}$$

In theory, the smaller N is, the less reactive power flows, but due to the limitation of the controller's response speed, N cannot be too small. Equation (12) provides a reference for the value of N. Through (10), the transmission power can be designed more accurately.

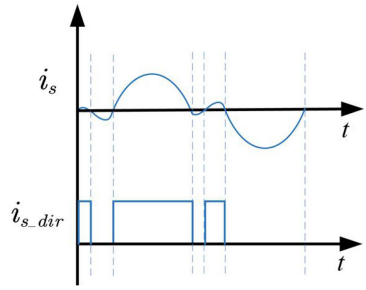

Fig. 10. i_s and its polarity signal i_{s_dir} when the harmonic current is too large.

C. Sensitivity of Control Strategy to Harmonics and Parameter Optimization Design

The implementation of the proposed strategy depends on the detection of the zero crossing point of i_s. However, the harmonic current not only affect θ, but also cause multiple zero crossings as Fig. 10 when the harmonic current is too large. Multiple zero crossings will cause the polarity signal i_{s_dir} to generate multiple rising edges in one switching cycle. This will cause phase

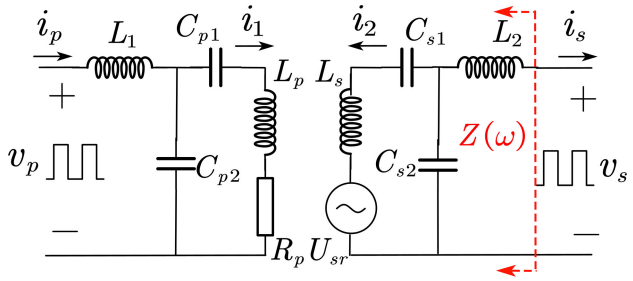

Fig. 11. Equivalent circuit of resonant network.

synchronization errors. Therefore, the harmonic model of i_s is needed to study the harmonic sensitivity of the control strategy.

Assuming that the phase of v_{s_1th} is 0, the fundamental current i_{s_1th} of i_s satisfy

$$i_{s\_1th} = \frac{MV_{p\_1th}}{\omega_0 L_1 L_2} \sin\left(\omega_0 t - \frac{\pi}{2} - \theta\right). \tag{13}$$

From (1), the harmonic voltage in v_s varies with θ_s. In order to calculate the harmonic current, it is necessary to calculate the input impedance of secondary resonant network. The equivalent circuit of compensation network is shown in Fig. 11. The secondary circuit is equivalent to resistance R_P at the primary side, and the primary circuit is equivalent to the fundamental voltage source U_{sr} at the secondary side. Due to the low-pass filtering characteristics of *LCC* resonant network, the power in L_P and L_S is mainly transferred by fundamental voltage and current. So R_P and U_{sr} are calculated using the fundamental model

$$\begin{cases} R_p = \dfrac{i_2 \omega_0 M j}{i_1} = k\omega_0 L_p \dfrac{V_{s\_1th}}{V_{p\_1th}} \\ U_{sr} = i_1\, \omega_0 M j = k\dfrac{L_p}{L_1} V_{p_{1th}} \sin(\omega_0 t) \end{cases}. \tag{14}$$

Ignoring U_{sr}, the harmonic input impedance $Z(\omega)$ of the secondary side can be calculated

$$Z(\omega) = j\omega L_2 + \frac{\frac{1}{j\omega C_{s2}}}{j\omega L_s + \frac{1}{j\omega C_{s1}}}. \tag{15}$$

In order to simplify the impedance, parameter a is introduced in this article in combination with (3)

$$a = \frac{P_{\max}}{V_{p\_1th} V_{s\_1th}} = \frac{k_0 L_p}{\omega_0 {L_1}^2} \tag{16}$$

where k_0 is the coupling coefficient of rated working distance and $P_{\max}$ is the designed rated power. a is a constant, reflecting the ability of the system to transmit power. Then, (17) is obtained by combining (15) and (16)

$$\begin{aligned} Z(n) &= \omega_0 L_1 * \frac{n^4 - 2n^2 + 1 - \frac{k_0}{a\omega_0 L_1}}{n^3 - n} j \\ &= |X_{L_1}| * \frac{n^4 - 2n^2 + 1 - \frac{k_0}{a|X_{L_1}|}}{n^3 - n} j \end{aligned} \tag{17}$$

where n is the harmonic order. According to (17), the input impedance is an inductor with a value of $|Z(n)|$ and the resonant

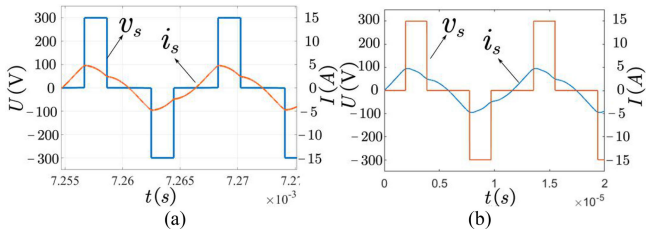

Fig. 12. Waveform of i_s when $k = 0.2$. (a) Simulation waveforms. (b) Analytical waveforms.

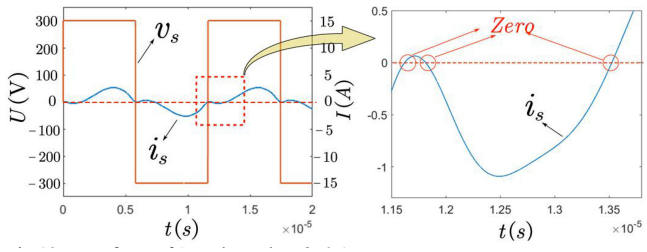

Fig. 13. Waveform of i_s and v_s when $k = 0.1$.

current i_s can be calculated as follows:

$$\begin{aligned} i_s(t) = &-I_{s\_1th} \sin\left(\omega_0 t - \theta + \frac{\pi}{2}\right) \\ &- \sum_{n=35\ldots}^{\infty} I_{s\_nth} \sin\left(n\omega_0 t - \frac{\pi}{2}\right) \end{aligned} \tag{18}$$

where

$$I_{s\_1th} = \frac{M}{\omega L_1 L_2} V_{p\_1th},\ I_{s\_nth} = \frac{V_{s\_nth}}{|Z(n)|} (n = 35\ldots)$$

In (18), parameter θ needs to be solved. According to the proposed control strategy, $i_s = 0$ at the synchronization point, so wehave $i_s(0) = 0$. Combining with (18), θ can be derived

$$\theta = -\frac{\pi}{2} + \arcsin\left(\frac{I_{s_{3th}} + I_{s_{5th}} + \cdots + I_{s_{nth}}}{I_{s_{1th}}}\right). \tag{19}$$

According to (19), when the harmonic current is 0, $\theta = -90°$. That is, when $\theta = -90°$, the reactive power is 0. This is the same as the conclusion deduced from (3). The harmonic current cause θ to deviate from $-90°$. Furthermore, both simulated and analytical waveforms of i_s are shown in Fig. 12. The analytical waveforms is consistent with the simulation results, which verifies the effectiveness of the model.

On the other hand, when the system is working, the induction coil may be dislocated and k decreases. Then, I_{s_1th} decreases. In order to maintain constant power output, θ_s decreases, so V_{s_nth} may increase and the harmonic current will increase. When $k = 0.1$, i_s is shown in Fig. 13. The harmonic currents cause multiple zero crossings in i_s. It will cause incorrect synchronization.

In summary, harmonic current will not only affect the value of θ, but also cause i_s to have multiple zero crossing points in serious cases, which greatly reduces the accuracy of detection. Therefore, it is necessary to reduce the harmonic current. The gain of harmonic current under different $|X_{L1}|$ is shown in

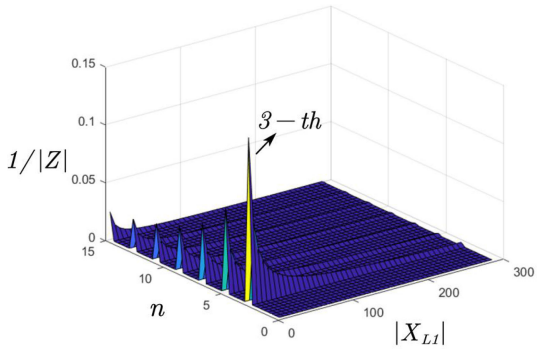

Fig. 14. Harmonic current gain varying with $|X_{L1}|$.

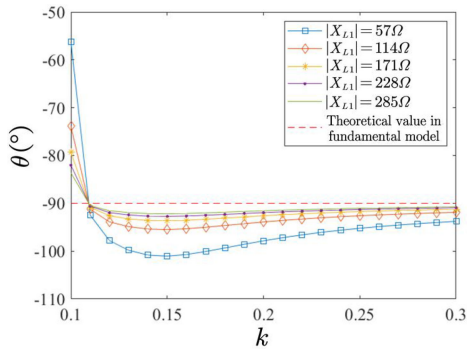

Fig. 15. Calculation of θ considering harmonics.

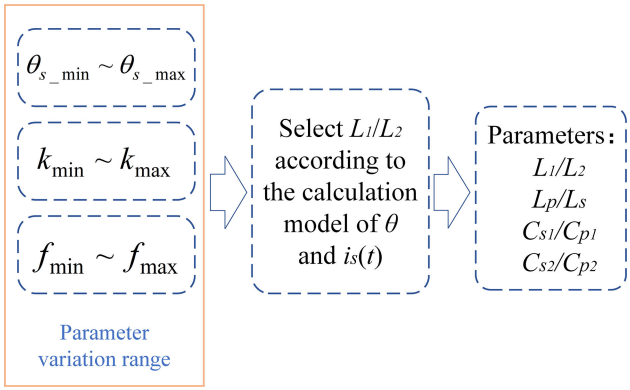

Fig. 16. Parameter selection.

Fig. 14. As $|X_{L1}|$ increases, the harmonic current gain decreases, but the trend gradually slows down. Therefore, it is not necessary to choose an excessively large $|X_{L1}|$.

When selecting different $|X_{L1}|$, the change of θ with k is shown in the Fig. 15. The larger the $|X_{L1}|$ is, the closer the θ is to the theoretical value of $-90°$. Therefore, the method of avoiding reactive power flow by keeping θ at $\pm 90°$ [29] is not reliable.

When designing the parameters, the resonant frequency needs to be determined first and its range is usually limited, so $|X_{L1}|$ can be increased by increasing L_1. However, when L_1 increases, the parasitic resistance increases, and the efficiency will decrease. Therefore, L_1 can not be too large. The parameter selection process is shown in Fig. 16, where θ_s is related to the power transmission range, k can be obtained from the transmission distance, and f is determined by the frequency tracking range of the primary controller. In order to avoid multiple zero crossing points in i_s, the worst working condition can be selected to design the minimum L_1/L_2 according to the proposed calculation model of i_s, and then other parameters can be obtained. The parameter selection principle takes into account the accuracy of control strategy detection and transmission efficiency.

TABLE II
COMPONENT PARAMETERS

Parameters	Value	Parameters	Value
C_{p2}, C_{s2}	33nF	R_{L1}, R_{L2}	0.21Ω
C_{p1}, C_{s1}	12nF	R_{Lp}, R_{Ls}	0.32Ω
L_1, L_2	108uH	Air gap	150mm
L_p, L_s	406uH	V_{DC1}, V_{DC2}	300V

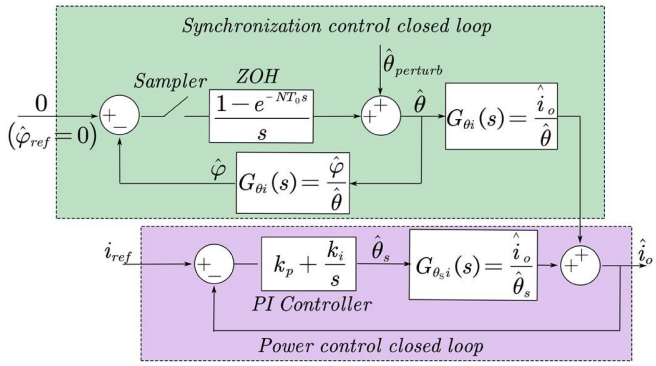

Fig. 17. Control block diagram.

D. Stability Analysis

After the analysis of harmonic sensitivity in Section III-C, a set of appropriate parameters are designed, as given in Table II. R_{L1}, R_{L2}, R_{Lp}, and R_{Ls} are the parasitic resistances of L_1, L_2, L_p, and L_s, respectively, and the rated transmission power is 1 kW.

In order to analyze the stability of the proposed control strategy, it is necessary to establish the small signal model of the control system and obtain the transfer function for analysis. The small signal model of the proposed control strategy is shown in Fig. 17, where

φ phase difference between v_s and i_s
φ_{ref} reference of φ
$G_{\theta i}$ open-loop transfer function between $\hat{\theta}$ and $\hat{i}_o$
$G_{\theta_s i}$ open-loop transfer function between $\hat{\theta}_s$ and $\hat{i}_o$
$G_{\theta\varphi}$ open-loop transfer function between $\hat{\theta}$ and $\hat{\varphi}$.

For a variable x, $\hat{x}$ represents its perturbation. The control block diagram is divided into synchronization control closed loop and power control closed loop. Correspondingly, the disturbance of output current i_o also comes from two parts: the disturbance caused by the change of θ and θ_s respectively. According to (4), when there is an error in the switching frequency between the primary and secondary side bridges, there

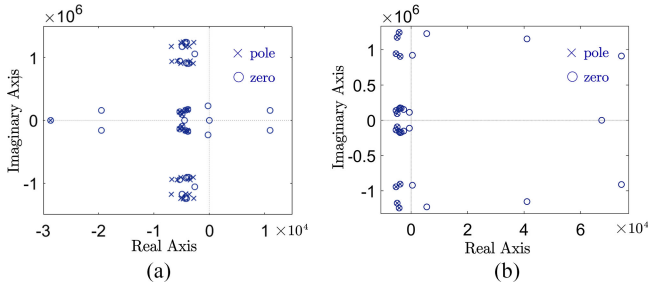

Fig. 18. Zero pole distribution of transfer function. (a) $G_{\theta_{\text{perturb}}i}$ (b) $G_{i_{\text{ref}}i}$.

is a continuous phase difference disturbance between v_p and v_s. The disturbance can be regarded as the perturbation $\hat{\theta}_{\text{perturb}}$ of θ in the small signal model. In the synchronous control closed loop, the purpose of synchronization is to keep φ at 0, so $\hat{\varphi}_{\text{ref}}$ is 0. The proposed control strategy synchronizes v_s every N cycles. It can be regarded as a discrete control with a period of NT_0, which can be equivalent to the sampler and zero order holder (ZOH) link. The sampler samples the error of φ every N cycles and generates the corrected value of θ after ZOH.

The closed-loop transfer function between $\hat{\theta}_{\text{perturb}}$ and $\hat{i}_o$ can be expressed as $G_{\theta_{\text{perturb}}i}$, and the closed-loop transfer function between $\hat{i}_{ref}$ and $\hat{i}_o$ can be expressed as $G_{i_{\text{ref}}i}$. According to Fig. 17, $\hat{i}_o$ can be expressed as

$$\begin{aligned}\hat{i}_o &= G_{\theta_{\text{perturb}}i}\hat{\theta}_{\text{perturb}} + G_{i_{\text{ref}}i}\hat{i}_{\text{ref}} \\ &= \frac{G_{\theta i}}{1 + G_{\theta\varphi}\frac{1-e^{-NTs}}{s}} * \frac{1}{1+\left(k_p+\frac{k_i}{s}\right)G_{\theta_s i}}\hat{\theta}_{\text{perturb}} \\ &\quad + \frac{\left(k_p+\frac{k_i}{s}\right)G_{\theta_s i}}{1+\left(k_p+\frac{k_i}{s}\right)G_{\theta_s i}}\hat{i}_{\text{ref}}. \end{aligned} \tag{20}$$

To obtain the closed-loop transfer function, it is necessary to establish the small signal model of the circuit to calculate $G_{\theta i}$, $G_{\theta_s i}$ and $G_{\theta\varphi}$. For resonant circuits, GSSA method is widely used to analyze dynamic characteristics. The compensation network port equations are established and the open-loop transfer functions are obtained by GSSA method. The details of the solution are shown in the Appendix. According to the small signal model, the zero pole distribution diagram of $G_{\theta_{\text{perturb}}i}$ and $G_{i_{\text{ref}}i}$ can be drawn, as shown in Fig. 18. The real parts of the poles are all negative, so the system can operate stably. The small signal model can also be used for control parameter design.

IV. Experimental Results

A BWPT prototype with rated power of 1 kW and resonant frequency of 84.27 kHz is designed and built. The source and load are both 300 V dc sources. The prototype is shown in Fig. 19.

A. Experimental Verification

When the circuit works, the ratio of ΔT to T_0 is 0.34%. As shown in Fig. 20, the output current i_o oscillates when the proposed synchronous control strategy is not adopted.

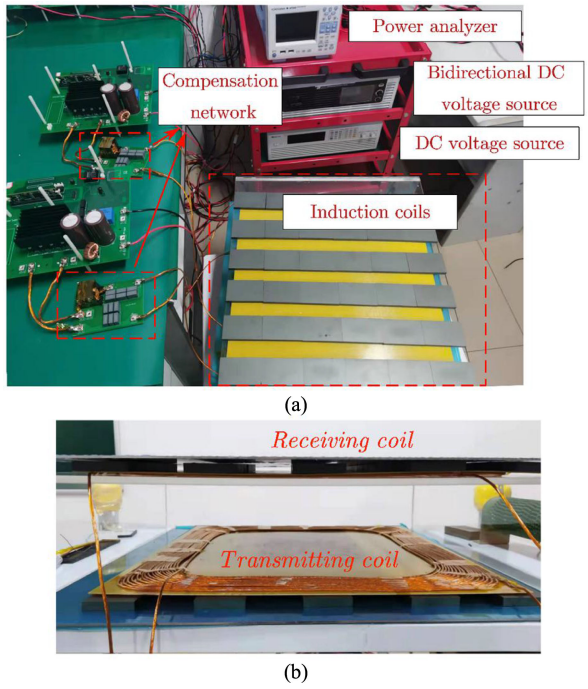

Fig. 19. Prototype image. (a) Prototype. (b)Induction coils.

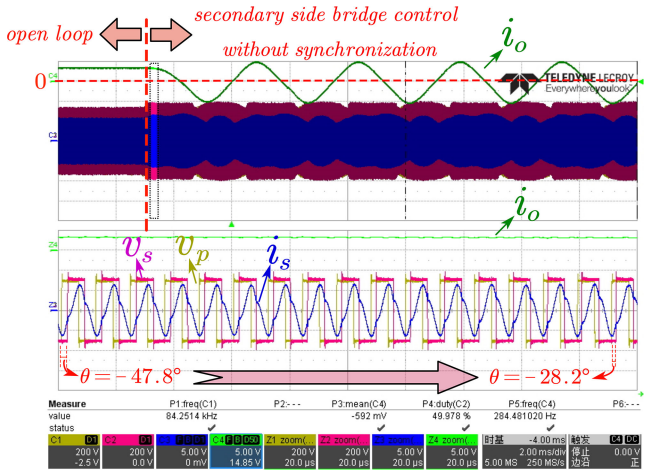

Fig. 20. Output current without using the proposed control strategy.

θ gradually changes under the influence of frequency difference. The oscillation frequency is 285 Hz, which is consistent with the theoretical value calculated by (5).

During oscillation, the phases of v_s and i_s are different, resulting in reactive power flow. As a comparison, the proposed control strategy is adopted and the number of synchronization cycles N is set to 6. Fig. 21 shows the operating waveform when the transmission power is 1 kW. θ_s is stable at 21°, and the efficiency reaches 94.27%. Fig. 21(a) shows the driving and drain source voltage of the primary side MOSFET. The primary side bridge realizes zero voltage switching ON. The voltage and current waveforms of the secondary side are given in Fig. 21(b). The phases of v_s and i_s are consistent and there is no reactive power flow. Affected by the harmonic current, the value of

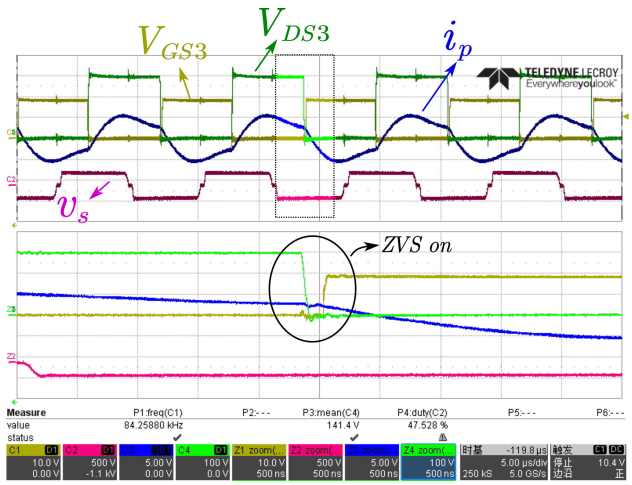

(a)

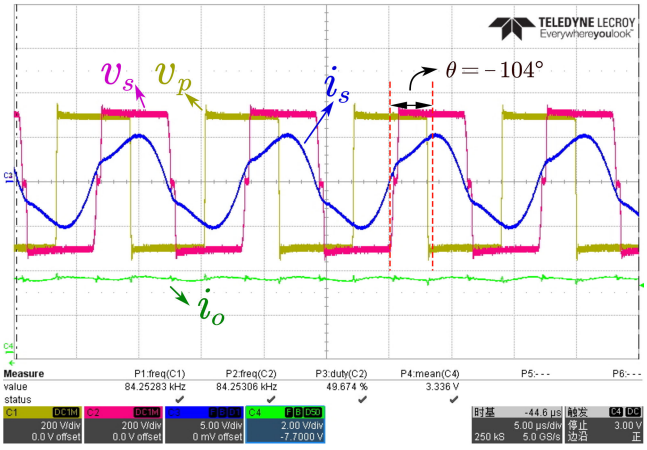

(b)

Fig. 21. Operating waveforms with output power of 1kW (adopting the proposed control strategy). (a) Primary side. (b) Secondary side.

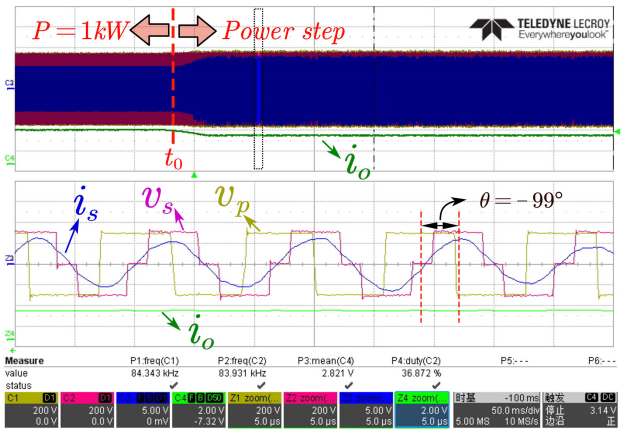

Fig. 22. Step response waveforms.

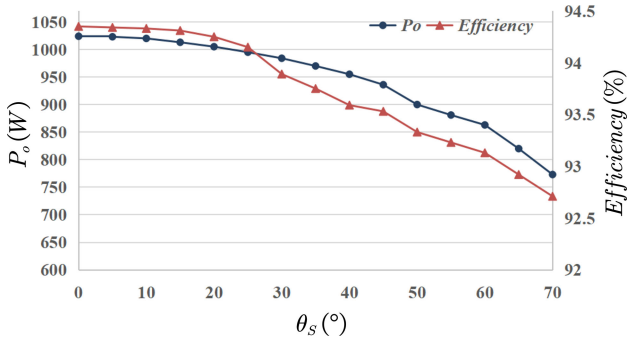

Fig. 23. Transmission power and efficiency.

θ is $-104°$, indicating that the effectiveness of the control strategy of maintaining $\theta = -90°$ by continuously detecting θ is insufficient.

In order to verify the stability of the dynamic working process, the dynamic waveforms of the step response are observed, as shown in Fig. 22. At t_0, the command signal with 850 W is given, and the system can respond effectively. In steady state, $i_o = 2.82$ A, $\theta_s = 53°$, $\theta = -99°$. i_o is constant and the phases of v_s and i_s are always the same, which proves the effectiveness of the control strategy. Due to the decrease of harmonic current caused by the increase of θ_s, θ is closer to $-90°$ compared with the value at 1 kW, which is consistent with the theoretical analysis in (19). Therefore, the value of θ is different under different transmission power. The proposed strategy can stabilize θ at an appropriate value at different power levels, that is, output constant power while keeping reactive power at 0.

Fig. 23 shows the transmission power and efficiency at different θ_s. The highest efficiency reaches 94.3%.

B. Robustness Test

To test the robustness of the proposed strategy, experiments are carried out under worse conditions. The frequency error is changed from 0.34% to 1%, and the effects of different synchronization cycles ($N = 4$, 6, 12) are tested under the condition of 1% frequency error. The operating waveform when $P_{\text{ref}} = 1$ kW is shown in Fig. 24. As shown in Fig. 24, the phases of v_s and i_s are the same, and the proposed strategy effectively controls i_o to be 3.3 A. As indicated in Fig. 24, the amplitude of i_s fluctuates slightly, and the fluctuation period is the same as T_C. The i_s with different N shows that the smaller T_C, the smaller the fluctuation, and the better the control effect.

Further, the experimental waveform when there is error in circuit parameters is shown in Fig. 25. The value of C_{s2} is changed to 26.4 nF to simulate the case where there is a 20% error between the component value and the design value. Compared with the case of $C_{s2} = 33$ nF, the maximum transmission power of the system is reduced to 850 W. The command signal from 850 to 800 W is given. In steady state, $\theta = -89°$, $\theta_s = 35°$. The system can still work effectively using the proposed strategy. The above experiments show that the control strategy has good robustness.

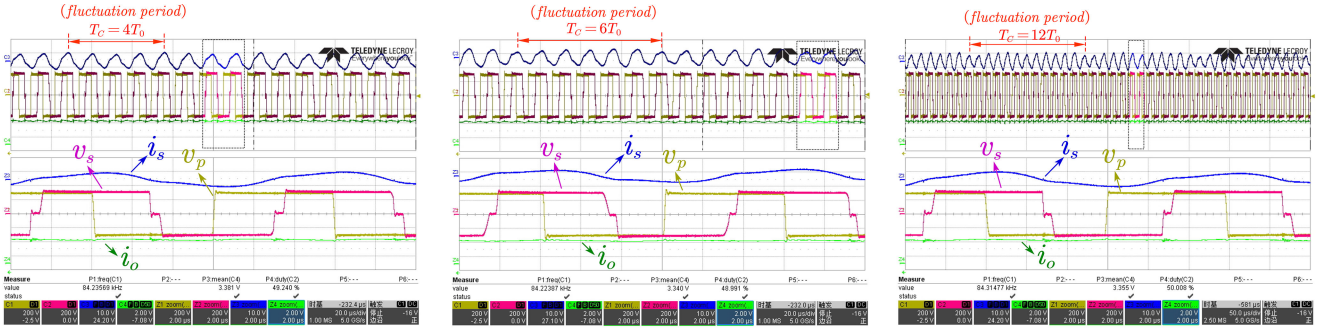

Fig. 24. Experimental waveforms with frequency error of 1%. (a) $N = 4$. (b) $N = 6$. (c) $N = 12$.

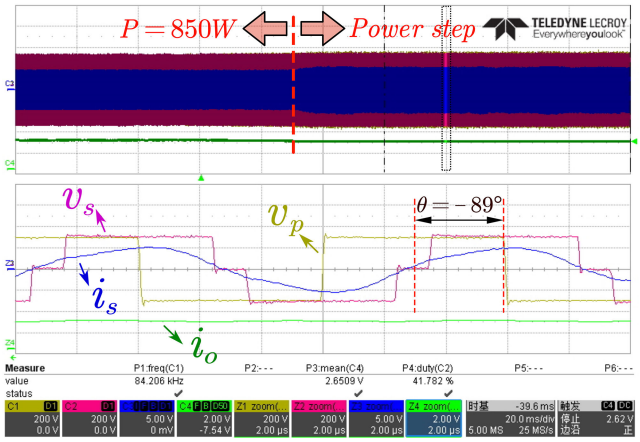

Fig. 25. Step response waveform at $C_{s2} = 26.4$ nF.

V. Conclusion

In this article, a constant power control strategy for the BWPT system without communication is proposed. The strategy solves the problems of reactive power flow and power oscillation caused by the change of relative phase angle. The switching sequence of the secondary side bridge is periodically synchronized according to the output current phase of the resonant network. Thus, it does not require reactive power closed loop and additional hardware, such as PLL or VCO. A mathematical model is established to analyze the current oscillation due to frequency deviation, and the design method of synchronization period is presented. Furthermore, the harmonic sensitivity analysis and parameter optimization design are carried out to improve the control efficiency. The stability of the proposed control strategy is proved with GSSA method. The simulation and experimental results of a 1 kW prototype verify the effectiveness of the proposed control strategy and mathematical model. The proposed strategy is not affected by parameter fluctuation while outputting constant current. Therefore, the proposed strategy is a simple and effective solution free of wireless communication.

Appendix

The solution process of open-loop transfer function is presented in this section. Selecting inductor currents and capacitor voltages as state variables, the *LCC-LCC* compensation network can be described as

$$\begin{cases} v_p = L_1 \dfrac{di_p}{dt} + v_{C_{p2}} + i_p R_{L1} \\ v_s = -L_2 \dfrac{di_s}{dt} + v_{C_{s2}} - i_s R_{L2} \\ i_p - i_1 = C_{p2} \dfrac{dv_{C_{p2}}}{dt} \\ -i_s - i_2 = C_{s2} \dfrac{dv_{C_{s2}}}{dt} \\ v_{C_{p2}} = v_{C_{p1}} + L_p \dfrac{di_1}{dt} + M \dfrac{di_2}{dt} + i_1 R_{Lp} \\ v_{C_{s2}} = v_{C_{s1}} + L_s \dfrac{di_2}{dt} + M \dfrac{di_1}{dt} + i_2 R_{Ls} \\ i_1 = C_{p1} \dfrac{dv_{C_{p1}}}{dt} \\ i_2 = C_{s1} \dfrac{dv_{C_{s1}}}{dt} \end{cases} . \tag{21}$$

where $v_{C_{p1}}$, $v_{C_{s1}}$, $v_{C_{p2}}$, and $v_{C_{s2}}$ are the voltages of C_{p1}, C_{s1}, C_{p2} and C_{s2} respectively. After the parameter optimization, the harmonic content in the system is low, and the energy transmission and dynamic characteristics are dominated by the fundamental component. Therefore, the fundamental frequency component is used to describe the dynamic characteristics of the system, v_p and v_s can be expressed as

$$\begin{cases} v_p = \dfrac{4V_{\mathrm{DC1}}}{\pi} \sin(\omega_0 t) \\ v_s = \dfrac{4V_{\mathrm{DC2}}}{\pi} \cos\dfrac{\theta_s}{2} \sin(\omega_0 t + \theta) \end{cases} . \tag{22}$$

For resonant circuits, GSSA method is widely used to analyze dynamic characteristics. In GSSA method, a variable $x(t)$ can be expressed as

$$x(t) = \langle x(t) \rangle_s \sin \omega t + \langle x(t) \rangle_c \cos \omega t \tag{23}$$

where $\langle x(t) \rangle_s$ and $\langle x(t) \rangle_c$ are the coefficients of sine component and cosine component of $x(t)$ Fourier expansion, respectively. (24) can be obtained by expressing all eight state variables in the form of (23).

In order to establish a small signal model, a variable x needs to be expressed as the addition of steady-state X and disturbance $\hat{x}$, as shown in (25)

$$\begin{cases}
\dfrac{4V_{\mathrm{DC1}}}{\pi} = L_1\left(\dfrac{\mathrm{d}\langle i_p\rangle_s}{\mathrm{dt}} - \omega_0\langle i_p\rangle_c\right) + \langle v_{C_{p2}}\rangle_s + \langle i_p\rangle_s R_{L1} \\
0 = L_1\left(\dfrac{\mathrm{d}\langle i_p\rangle_c}{\mathrm{dt}} + \omega_0\langle i_p\rangle_s\right) + \langle v_{C_{p2}}\rangle_c + \langle i_p\rangle_c R_{L1} \\
\dfrac{4V_{\mathrm{DC2}}}{\pi}\cos\dfrac{\theta_s}{2}\cos\theta = -L_2\left(\dfrac{d\langle i_s\rangle_s}{dt} - \omega_0\langle i_s\rangle_c\right) + \langle v_{C_{s2}}\rangle_s - \langle i_s\rangle_s R_{L2} \\
\dfrac{4V_{\mathrm{DC2}}}{\pi}\cos\dfrac{\theta_s}{2}\sin\theta = -L_2\left(\dfrac{d\langle i_s\rangle_c}{dt} + \omega_0\langle i_s\rangle_s\right) + \langle v_{C_{s2}}\rangle_c - \langle i_s\rangle_c R_{L2} \\
\langle i_p\rangle_s - \langle i_1\rangle_s = C_{p2}\left(\dfrac{\mathrm{d}\langle v_{C_{p2}}\rangle_s}{\mathrm{dt}} - \omega_0\langle v_{C_{p2}}\rangle_c\right) \\
\langle i_p\rangle_c - \langle i_1\rangle_c = C_{p2}\left(\dfrac{d\langle v_{C_{p2}}\rangle_c}{dt} + \omega_0\langle v_{C_{p2}}\rangle_s\right) \\
-\langle i_s\rangle_s - \langle i_2\rangle_s = C_{s2}\left(\dfrac{\mathrm{d}\langle \mathrm{v}_{C_{s2}}\rangle_s}{dt} - \omega_0\langle v_{C_{s2}}\rangle_c\right) \\
-\langle i_2\rangle_c - \langle i_s\rangle_c = C_{s2}\left(\dfrac{d\langle v_{C_{s2}}\rangle_c}{dt} + \omega_0\langle v_{C_{s2}}\rangle_s\right) \\
\langle v_{C_{p2}}\rangle_s = \langle v_{C_{p1}}\rangle_s + L_p\left(\dfrac{d\langle i_1\rangle_s}{dt} - \omega_0\langle i_1\rangle_c\right) + M\left(\dfrac{\mathrm{d}\langle i_2\rangle_s}{dt} - \omega_0\langle i_2\rangle_c\right) + \langle i_1\rangle_s R_{Lp} \\
\langle v_{C_{p2}}\rangle_c = \langle v_{C_{p1}}\rangle_c + L_p\left(\dfrac{d\langle i_1\rangle_c}{dt} + \omega_0\langle i_1\rangle_s\right) + M\left(\dfrac{\mathrm{d}\langle i_2\rangle_c}{dt} + \omega_0\langle i_2\rangle_s\right) + \langle i_1\rangle_c R_{Lp} \\
\langle v_{C_{s2}}\rangle_s = \langle v_{C_{s1}}\rangle_s + L_s\left(\dfrac{d\langle i_2\rangle_s}{dt} - \omega_0\langle i_2\rangle_c\right) + M\left(\dfrac{\mathrm{d}\langle i_1\rangle_s}{\mathrm{dt}} - \omega_0\langle i_1\rangle_c\right) + \langle i_2\rangle_s R_{Ls} \\
\langle v_{C_{s2}}\rangle_c = \langle v_{C_{s1}}\rangle_c + L_s\left(\dfrac{d\langle i_2\rangle_c}{dt} + \omega_0\langle i_2\rangle_s\right) + M\left(\dfrac{\mathrm{d}\langle i_1\rangle_c}{dt} + \omega_0\langle i_1\rangle_s\right) + \langle i_2\rangle_c R_{Ls} \\
\langle i_1\rangle_s = C_{p1}\left(\dfrac{d\langle v_{C_{p1}}\rangle_s}{dt} - \omega_0\langle v_{C_{p1}}\rangle_c\right) \\
\langle i_1\rangle_c = C_{p1}\left(\dfrac{d\langle v_{C_{p1}}\rangle_c}{dt} + \omega_0\langle v_{C_{p1}}\rangle_s\right) \\
\langle i_2\rangle_s = C_{s1}\left(\dfrac{d\langle v_{C_{s1}}\rangle_s}{dt} - \omega_0\langle v_{C_{s1}}\rangle_c\right) \\
\langle i_2\rangle_c = C_{s1}\left(\dfrac{d\langle v_{C_{s1}}\rangle_c}{dt} + \omega_0\langle v_{C_{s1}}\rangle_s\right)
\end{cases} \tag{24}$$

$$x = X + \hat{x} \tag{25}$$

$$\begin{cases}
0 = L_1\left(\dfrac{\mathrm{d}\langle \hat{i}_p\rangle_s}{\mathrm{dt}} - \omega_0\langle \hat{i}_p\rangle_c\right) + \langle \hat{v}_{C_{p2}}\rangle + \langle \hat{i}_p\rangle_s R_{L1} \\
0 = L_1\left(\dfrac{\mathrm{d}\langle \hat{i}_p\rangle_c}{\mathrm{dt}} + \omega_0\langle \hat{i}_p\rangle_s\right) + \langle \hat{v}_{C_{p2}}\rangle_c + \langle \hat{i}_p\rangle_c R_{L1} \\
\quad -\dfrac{4V_{\mathrm{DC2}}}{\pi}\left(\dfrac{\hat{\theta}_s}{2}\cos\theta\sin\dfrac{\theta_s}{2} + \hat{\theta}\cos\dfrac{\theta_s}{2}\sin\theta\right) \\
= -L_2\left(\dfrac{d\langle \hat{i}_s\rangle_s}{dt} - \omega_0\langle \hat{i}_s\rangle_c\right) + \langle \hat{v}_{C_{s2}}\rangle_s - \langle \hat{i}_s\rangle_s R_{L2} \\
\quad \dfrac{4V_{\mathrm{DC2}}}{\pi}\left(-\dfrac{\hat{\theta}_s}{2}\sin\theta\sin\dfrac{\theta_s}{2} + \hat{\theta}\cos\dfrac{\theta_s}{2}\cos\theta\right) \\
= -L_2\left(\dfrac{\mathrm{d}\langle \hat{\mathrm{i}}_s\rangle_c}{\mathrm{dt}} + \omega_0\langle \hat{i}_s\rangle_s\right) + \langle \hat{v}_{C_{s2}}\rangle_c - \langle \hat{i}_s\rangle_c R_{L2} \\
\langle \hat{i}_p\rangle_s - \langle \hat{i}_1\rangle_s = C_{p2}\left(\dfrac{d\langle \hat{v}_{C_{p2}}\rangle_s}{dt} - \omega_0\langle \hat{v}_{C_{p2}}\rangle_c\right) \\
\langle \hat{i}_p\rangle_c - \langle \hat{i}_1\rangle_c = C_{p2}\left(\dfrac{d\langle \hat{v}_{C_{p2}}\rangle_c}{dt} + \omega_0\langle \hat{v}_{C_{p2}}\rangle_s\right) \\
-\langle \hat{i}_2\rangle_s - \langle \hat{i}_s\rangle_s = C_{s2}\left(\dfrac{d\langle \hat{v}_{C_{s2}}\rangle_s}{dt} - \omega_0\langle \hat{v}_{C_{s2}}\rangle_c\right) \\
-\langle \hat{i}_2\rangle_c - \langle \hat{i}_s\rangle_c = C_{s2}\left(\dfrac{d\langle \hat{v}_{C_{s2}}\rangle_c}{dt} + \omega_0\langle \hat{v}_{C_{s2}}\rangle_s\right) \\
\langle \hat{v}_{C_{p2}}\rangle_s = \langle \hat{v}_{C_{p1}}\rangle_s + L_p\left(\dfrac{d\langle \hat{i}_1\rangle_s}{dt} - \omega_0\langle \hat{i}_1\rangle_c\right) + M\left(\dfrac{d\langle \hat{i}_2\rangle_s}{dt} - \omega_0\langle \hat{i}_2\rangle_c\right) + \langle \hat{i}_1\rangle_s R_{Lp} \\
\langle \hat{v}_{C_{p2}}\rangle_c = \langle \hat{v}_{C_{p1}}\rangle_c + L_p\left(\dfrac{d\langle \hat{i}_1\rangle_c}{dt} + \omega_0\langle \hat{i}_1\rangle_s\right) + M\left(\dfrac{d\langle \hat{i}_2\rangle_c}{dt} + \omega_0\langle \hat{i}_2\rangle_s\right) + \langle \hat{i}_1\rangle_c R_{Lp} \\
\langle \hat{v}_{C_{s2}}\rangle_s = \langle \hat{v}_{C_{s1}}\rangle_s + L_s\left(\dfrac{d\langle \hat{i}_2\rangle_s}{dt} - \omega_0\langle \hat{i}_2\rangle_c\right) + M\left(\dfrac{d\langle \hat{i}_1\rangle_s}{dt} - \omega_0\langle \hat{i}_1\rangle_c\right) + \langle \hat{i}_2\rangle_s R_{Ls} \\
\langle \hat{v}_{C_{s2}}\rangle_c = \langle \hat{v}_{C_{s1}}\rangle_c + L_s\left(\dfrac{\mathrm{d}\langle \hat{i}_2\rangle_c}{dt} + \omega_0\langle \hat{i}_2\rangle_s\right) + M\left(\dfrac{d\langle \hat{i}_1\rangle_{sc}}{dt} + \omega_0\langle \hat{i}_1\rangle_{ss}\right) + \langle \hat{i}_2\rangle_c R_{Ls} \\
\langle \hat{i}_1\rangle_s = C_{p1}\left(\dfrac{d\langle \hat{v}_{C_{p1}}\rangle_s}{dt} - \omega_0\langle \hat{v}_{C_{p1}}\rangle_c\right) \\
\langle \hat{i}_1\rangle_c = C_{p1}\left(\dfrac{d\langle \hat{v}_{C_{p1}}\rangle_c}{dt} + \omega_0\langle \hat{v}_{C_{p1}}\rangle_s\right) \\
\langle \hat{i}_2\rangle_s = C_{s1}\left(\dfrac{d\langle \hat{v}_{C_{s1}}\rangle_s}{dt} - \omega_0\langle \hat{v}_{C_{s1}}\rangle_c\right) \\
\langle \hat{i}_2\rangle_c = C_{s1}\left(\dfrac{d\langle \hat{v}_{C_{s1}}\rangle_c}{dt} + \omega_0\langle \hat{v}_{C_{s1}}\rangle_s\right).
\end{cases} \tag{26}$$

The input disturbances in the system are $\hat{\theta}$ and $\hat{\theta}_s$. By substituting all variables as shown in (25), (24) can be rewritten in a linear small-signal form as (26).

Equation (26) reflects the dynamic characteristics of state variables. In order to solve the transfer function, the output equation needs to be established. The phase θ_{is} of i_s satisfies

$$\tan\theta_{is} = \frac{i_{sc}}{i_{ss}}. \tag{27}$$

Then , $\hat{\varphi}$ can be solved

$$\hat{\varphi} = \hat{\theta} - \hat{\theta}_{is} = \hat{\theta} - \frac{1}{\langle i_s\rangle_s + \langle i_s\rangle_c \tan\,\theta_{is}}\langle\hat{i}_s\rangle_c + \frac{\tan\,\theta_{is}}{\langle i_s\rangle_s + \langle i_s\rangle_c \tan\,\theta_{is}}\langle\hat{i}_s\rangle_s. \tag{28}$$

Assuming that the amplitude of i_s is i_{sp}, ([29]) can be deduced according to the power conservation on both sides of the secondary side bridge

$$\begin{cases} {i_{sp}}^2 = {\langle i_s\rangle_s}^2 + {\langle i_s\rangle_c}^2 \\ \dfrac{i_{sp}}{\sqrt{2}} * \dfrac{V_{s\_1th}}{\sqrt{2}} * \cos\varphi = V_{DC2}\, i_o \end{cases} \tag{29}$$

$$\hat{i}_o = \frac{2}{\pi}\left[\cos\,\frac{\theta_s}{2}\cos\,\varphi\left(\frac{\langle i_s\rangle_s}{i_{sp}}\langle\hat{i}_s\rangle_s + \frac{\langle i_s\rangle_c}{i_{sp}}\langle\hat{i}_s\rangle_c\right) - \frac{1}{2}\sin\,\frac{\theta_s}{2}\cos\,\varphi i_{sp}\hat{\theta}_s - \sin\,\varphi\cos\,\frac{\theta_s}{2} i_{sp}\hat{\varphi}\right]. \tag{30}$$

Then, $\hat{i}_o$ can be solved as (30). In summary, the state equation of the compensation network can be expressed as

$$\begin{cases} \dot{\hat{x}} = A\hat{x} + B\hat{u} \\ \hat{y} = C\hat{x} + D\hat{u} \end{cases} \tag{31}$$

where

$$\hat{x} = \left[\langle\hat{i}_p\rangle_s\ \langle\hat{i}_p\rangle_c\langle\hat{i}_s\rangle_s\ \langle\hat{i}_s\rangle_c\ \langle\hat{v}_{C_{p2}}\rangle_s\langle\hat{v}_{C_{p2}}\rangle_c\ \langle\hat{v}_{C_{s2}}\rangle_s\langle\hat{v}_{C_{s2}}\rangle_c\langle\hat{i}_1\rangle_s\langle\hat{i}_1\rangle_c\langle\hat{i}_2\rangle_s\langle\hat{i}_2\rangle_c\ \langle\hat{v}_{C_{p1}}\rangle_s\langle\hat{v}_{C_{p1}}\rangle_c\langle\hat{v}_{C_{s1}}\rangle_s\langle\hat{v}_{C_{s1}}\rangle_c\right]^T$$

$$\hat{u} = \left[\hat{\theta}\ \hat{\theta}_s\right]^T$$

$$\hat{y} = \left[\hat{\varphi}\ \left|\hat{i}_o\right|\right]^T$$

A, B, C. and D are constants related to circuit parameters, which can be calculated according to (21)–(30). Then $G_{\theta i}$, $G_{\theta_s i,}$ and $G_{\theta\varphi}$ can be calculated with the formula $C(sI - A)^{-1}B + D$.

ACKNOWLEDGMENT

The author would like to thank TDK corporation for providing materials and components for the research. They would like to thank PLEXIM Inc. for the support of the powerful simulation tools PLECS. They would like to thank Microgrid Electrical Equipment and Manufacture Platform (MEEMP) in the Polytechnic Institute of Zhejiang University, on which many valuable tests in this article were performed.

REFERENCES

[1] S. R. Khutwad and S. Gaur, "Wireless charging system for electric vehicle," in *Proc. Int. Conf. Signal Process., Commun., Power Embedded Syst.*, 2016, pp. 441–444.
[2] B. Li, M. Chen, X. Wang, N. Chen, X. Sun, and D. Zhang, "An optimized digital synchronous rectification scheme based on Time-domain model of resonant CLLC circuit," *IEEE Trans. Power Electron.*, vol. 36, no. 9, pp. 10933–10948, Dec. 2020.
[3] X. Wang *et al.*, "Control and modulation of a single-phase AC/DC converter with smooth bidirectional mode switching and symmetrical decoupling voltage compensation," *IEEE Trans. Power Electron.*, vol. 37, no. 4, pp. 3836–3853, Apr. 2022.
[4] N. Chen *et al.*, "Synchronous rectification based on resonant inductor voltage for CLLC bidirectional converter," *IEEE Trans. Power Electron.*, vol. 37, no. 1, pp. 547–561, Jan. 2022.
[5] A. Ahmad, M. Saad Alam, and R. Chabaan, "A comprehensive review of wireless charging technologies for electric vehicles," *IEEE Trans. Transp. Electrific.*, vol. 4, no. 1, pp. 38–63, Mar. 2018.
[6] P. K. Joseph, E. Devaraj, and A. Gopal, "Overview of wireless charging and vehicle-to-grid integration of electric vehicles using renewable energy for sustainable transportation," *IET Power Electron.*, vol. 12, pp. 627–638, 2019.
[7] M. Fu, C. Ma, and X. Zhu, "A cascaded boost-buck converter for high-efficiency wireless power transfer systems," *IEEE Trans. Ind. Inform.*, vol. 10, no. 3, pp. 1972–1980, Aug. 2014.
[8] K. Colak, M. Bojarski, E. Asa, and D. Czarkowski, "A constant resistance analysis and control of cascaded buck and boost converter for wireless EV chargers," in *Proc. IEEE Conf. Appl. Power Electron. Expo.*, 2015, pp. 3157–3161, doi: 10.1109/APEC.2015.7104803.
[9] A. Ting Leung Lee, W. Jin, and S.-C. Tan, "Buck-Boost single-inductor multiple-output high-frequency inverters for medium-power wireless power transfer," *IEEE Trans. Power Electron.*, vol. 34, no. 4, pp. 3457–3473, Apr. 2019.
[10] L. Jou, J. -C. Wu, K. -D. Wu, and C. -Y. Kuo, "Bidirectional DC–DC wireless power transfer based on LCC-C resonant compensation," *IEEE Trans. Power Electron.*, vol. 36, no. 2, pp. 2310–2319, Feb. 2021.
[11] B. X. Nguyen and D. M. Vilathgamuwa, "An efficiency optimization scheme for bidirectional inductive power transfer systems," *IEEE Trans. Power Electron.*, vol. 30, no. 11, pp. 6310–6318, Nov. 2015.
[12] H. G. Park *et al.*, "A design of a wireless power receiving unit with a high-efficiency 6.78-MHz active rectifier using shared DLLs for magnetic-resonant A4WP applications," *IEEE Trans. Power Electron.*, vol. 31, no. 6, pp. 4484–4498, Jun. 2016.
[13] L. Cheng, W. Ki, Y. Lu, and T. Yim, "Adaptive on/off delay-compensated active rectifiers for wireless power transfer systems," *IEEE J. Solid-State Circuits*, vol. 51, no. 3, pp. 712–723, Mar. 2016.
[14] A. A. S. Mohamed, A. Berzoy, and O. Mohammed, "Experimental validation of comprehensive steady-state analytical model of bidirectional WPT system in EVs applications," *IEEE Trans. Power Electron.*, vol. 66, no. 7, pp. 5584–5594, Jul. 2017.
[15] A. Berger, M. Agostinelli, and S. Vesti, "A wireless charging system applying phase-shift and amplitude control to maximize efficiency and extractable power," *IEEE Trans. Power Electron.*, vol. 30, no. 11, pp. 6338–6348, Nov. 2015.
[16] F. Liu, K. Li, and K. Chen, "A phase synchronization technique based on perturbation and observation for bidirectional wireless power transfer system," *IEEE J. Emerg. Sel. Topics Power Electron.*, vol. 8, no. 2, pp. 1287–1297, Jun. 2020.
[17] P. O'Neill, J. Zhang, and W. G. Hurley, "A Phase-shifted full-bridge ZVS DC/DC converter for wireless charging of electric vehicles," in *Proc. 50th Int. Univ. Power Eng. Conf.*, 2015, pp. 1–5, doi: 10.1109/UPEC.2015.7339918.
[18] Z. Li and K. Song, "Constant current charging and maximum efficiency tracking control scheme for supercapacitor wireless charging," *IEEE Trans. Power Electron.*, vol. 33, no. 10, pp. 9088–9100, Oct. 2018.
[19] Y. Guo, Y. Zhang, and S. Li, "Load parameter joint identification of wireless power transfer system based on the DC input current and phase-shift angle," *IEEE Trans. Power Electron.*, vol. 35, no. 10, pp. 10542–10533, Oct. 2020.
[20] A. T. Cabrera, J. A. Aguado Sánchez, M. Longo, and F. Foiadelli, "Sensitivity analysis of a bidirectional wireless charger for EV," in *Proc. Int. Conf. Renew. Energy Res. Appl.*, 2016, pp. 1113–1116, doi: 10.1109/ICRERA.2016.7884506.

[21] T. Mizuno, S. Yachi, and A. Kamiya, "Improvement in efficiency of wireless power transfer of magnetic resonant coupling using magnetoplated wire," *IEEE Trans. Magn.*, vol. 47, no. 10, pp. 4445–4448, Oct. 2011.
[22] W. Zhang and C. C. Mi, "Compensation topologies of high-power wireless power transfer systems," *IEEE Trans. Veh. Technol.*, vol. 65, no. 6, pp. 4768–4778, Jun. 2016.
[23] J.-H. Lu, W.-J. Li, B. Li, and G.-R. Zhu, "Variable compensation network for achieving constant current or voltage output in IPT system," in *Proc. Int. Conf. Ind. Inform. Comput. Technol., Intell. Technol., Ind. Inf. Integr.*, 2016, pp. 14–17, doi: 10.1109/ICIICII.2016.0015.
[24] W. Zhong and S. Y. Ron Hui, "Charging time control of wireless power transfer systems without using mutual coupling information and wireless communication system," *IEEE Trans. Ind. Electron.*, vol. 64, no. 1, pp. 228–235, Jan. 2017.
[25] U. K. Madawala and M. Neath, "A power–frequency controller for bidirectional inductive power transfer systems," *IEEE Trans. Ind. Electron.*, vol. 60, no. 1, pp. 310–317, Jan. 2013.
[26] K. Song, Z. Li, and J. Jiang, "Constant current/voltage charging operation for series–series and series–parallel compensated wireless power transfer systems employing primary-side controller," *IEEE Trans. Power Electron.*, vol. 33, no. 9, pp. 8065–8080, Sep. 2018.
[27] F. Mao, Y. Lu, and R. P. Martins, "A reconfigurable cross-connected wireless-power transceiver for bidirectional Device-to-Device wireless charging," *IEEE J. Solid-State Circuits*, vol. 54, no. 9, pp. 2579–2589, Sep. 2019.
[28] X. Li, C.-Y. Tsui, and W.-H. Ki, "A 13.56 MHz wireless power transfer system with reconfigurable resonant regulating rectifier and wireless power control for implantable medical devices," *IEEE J. Solid-State Circuits*, vol. 50, no. 4, pp. 978–989, Apr. 2015.
[29] D. J. Thrimawithana, U. K. Madawala, and M. Neath, "A synchronization technique for bidirectional IPT systems," *IEEE Trans. Ind. Electron.*, vol. 60, no. 1, pp. 301–309, Jan. 2013.
[30] Y. Tang, Y. Chen, and U. K. Madawala, "A new controller for bidirectional wireless power transfer systems," *IEEE Trans. Power Electron.*, vol. 33, no. 10, pp. 9076–9087, Oct. 2018.
[31] D. J. Thrimawithana, U. K. Madawala, and M. Neath, "A P&Q based synchronization technique for bi-directional IPT pick-ups," in *Proc. IEEE 9th Int. Conf. Power Electron. Drive Syst.*, Dec. 2011, pp. 40–45.
[32] T. Tan, K. Chen, Y. Jiang, Q. Lin, L. Yuan, and Z. Zhao, "A bidirectional wireless power transfer system control strategy independent of real-time wireless communication," *IEEE Trans. Ind. Appl.*, vol. 56, no. 2, pp. 1587–1598, Mar./Apr. 2020.
[33] W. Zhang and C. C. Mi, "Compensation topologies of high-power wireless power transfer systems," *IEEE Trans. Veh. Technol.*, vol. 65, no. 6, pp. 4768–4778, Jun. 2016.
[34] S. Li, W. Li, J. Deng, T. D. Nguyen, and C. C. Mi, "A double-sided LCC compensation network and its tuning method for wireless power transfer," *IEEE Trans. Veh. Technol.*, vol. 64, no. 6, pp. 2261–2273, Jun. 2015.

Dongbo Zhang received the B.S. degree in electrical engineering in 2020 from Zhejiang University, Hangzhou, China, where he is currently working toward the M.S. degree in electrical engineering.

His research interests include wireless power transmission and high efficiency converters for renewable energy.

Min Chen (Member, IEEE) received the B.S. degree in applied electronics and the Ph.D. degree in electrical engineering from Zhejiang University, Hangzhou, China, in 2000 and 2006, respectively.

From 2007 to 2009, he was a Postdoctoral Researcher with the Department of Electrical Engineering, Zhejiang University. From 2010 to 2014, he was a Lecture, and in 2014 was promoted as an Associate Professor. Since 2020, he has been a Full Professor with Zhejiang University. From 2014 to 2015, he was a Visiting Researcher with the Department of Energy Technology, Aalborg University. He has authored or coauthored more than 80 SCI/EI-indexed papers and was issued for almost 30 patents of inventions. He is currently the Director of ZJU Joint Research Center for New Energy and Power Electronics Based Power System and the Deputy Director of the National Engineering Research center For Applied Power Electronics. His research interests include application of power electronics in power system, inverter and its control, renewable energy generation and grid connection, bidirectional energy conversion technology for electric vehicle energy storage and charging.

Bodong Li received the B.S. degree in electrical engineering from Yanshan University, Qinhuangdao, China, in 2016, and the M.S. degree in electrical engineering from Zhejiang University, Hangzhou, China, in 2020. He is currently working toward a Ph.D. degree in the college of electrical engineering, Zhejiang University, Hangzhou, China.

His research interests include high efficiency DC/DC converters, energy storage systems, photovoltaic and microgrid systems.

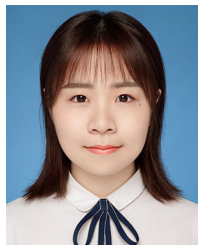

Xiaoqing Wang (Student Member, IEEE) received the B.S. degree in electrical engineering from the China University of Mining and Technology, Xuzhou, China, in 2017. She is currently working toward the Ph.D. degree with the College of Electrical Engineering, Zhejiang University, Hangzhou, China.

Her research interests include energy storage systems, power decoupling and high efficiency ac/dc converters.

Xinnan Sun received the B.E. degree in electrical engineering in 2019 from Zhejiang University, Hangzhou, China, where she is currently working toward the Ph.D degree with the College of electrical engineering, Zhejiang University.

Her research interests include bidirectional dc/dc converters and power modules.

Feng Jiang was born in Anhui Province, China. He received the master degree in electrical engineering from Zhejiang University, Hangzhou, China, in 2019. He is an Assistant Researcher with the College of Electrical Engineering, Zhejiang University. His special fields of interest included microgrid controller, application of power electronics in power system and renewable energy.